Dynamics of black hole apparent horizons

Peter Anninos,[1] David Bernstein,[1,3,*] Steven R. Brandt,[1,3] David Hobill,[1,2] Edward Seidel,[1,3] and Larry Smarr[1,3]
[1] *National Center for Supercomputing Applications, 605 E. Springfield Ave., Champaign, Illinois 61820*
[2] *Department of Physics and Astronomy, University of Calgary, Calgary, Alberta, Canada T2N 1N4*
[3] *Department of Physics, University of Illinois at Urbana-Champaign, Urbana, Illinois 61801*
(Received 30 March 1994)

Dynamic black hole spacetimes are studied by examining the evolution of apparent horizons surrounding the holes. We performed numerical evolutions of three different initial data sets: nonrotating black holes distorted by time symmetric (Brill) gravitational waves, distorted rotating black holes, and the time symmetric two black hole Misner data. Although the initial data sets represent different physical problems, the results for these systems are strikingly similar. At early times in the evolution, the apparent horizons may be very distorted and nonspherical (or disjoint in the case of two black holes), but the systems quickly settle down to a nearly spherical or oblate (in the case of rotating holes) configuration and the horizons are then seen to oscillate at the quasinormal frequency of the final black hole. In the case of two black holes with disjoint horizons, we see the appearance of a larger horizon surrounding both holes as they collide. From this point the horizon dynamics is very similar to the single distorted black hole systems. The wavelength and damping time of the quasinormal modes and the rotation parameter in the rotating cases can be read off directly from oscillations in the geometry of the black hole horizons. The apparent horizon is thus shown to be a powerful tool in the study of black hole spacetimes.

PACS number(s): 04.30.Db, 04.20.Ex, 04.25.Dm, 04.70.Bw

I. INTRODUCTION

The event horizon is the defining characteristic of a black hole. It marks the boundary separating the region where information is trapped inside the black hole from the region that is causally connected to future null infinity. For analytic black hole spacetimes, such as the Schwarzschild and Kerr solutions it is possible to compute the exact location of the horizon. However, these spacetimes are static or at least stationary, and therefore the horizons do not change in time. For more general spacetimes, Hawking has proved a very general principle that the surface area of the horizon must be a nondecreasing function of time [1], so that in dynamic situations the horizon will tend to grow as the hole swallows matter and energy. However, this powerful theorem does not provide any details of the specific dynamics of a black hole that has been distorted in some way. Therefore, an important issue to investigate in detail is how horizons of dynamic black hole spacetimes evolve in time.

The *apparent* horizon is defined to be the outermost trapped surface surrounding a black hole, and can be computed on any given Cauchy slice of the spacetime (see Sec. IV for more details). It is therefore more convenient for numerical computation than the actual event horizon which can be known only by considering the future evolution of the spacetime. The apparent horizon is known either to lie inside or to coincide with the event horizon. In a recent paper [2] we compared the dynamics of event and apparent horizons for a number of black hole spacetimes. Here we wish to pursue the use of the apparent horizon as a powerful tool for studying numerically generated black hole spacetimes. Detailed studies of the event horizons in these spacetimes will be discussed elsewhere.

As we detail below, studies of the apparent horizon of a black hole can reveal its oscillation frequency, mass, and angular momentum. Even very strongly distorted black hole horizons are seen to quickly settle in to configurations that oscillate about an equilibrium shape at the lowest quasinormal frequency of the black hole. The intrinsic geometric shape (as distinct from the less relevant *coordinate* shape) of the equilibrium apparent horizon has a fairly sensitive dependence on the angular momentum of the hole. It is spherical for a nonrotating black hole and progressively more oblate for black holes with more and more angular momentum. The horizon itself can be used as a probe to determine the rotation of the hole even in the regime where the wavelength and damping time of the quasinormal mode are virtually indistinguishable from a nonrotating black hole. These properties of the horizon are shown in detail in the sections below, and are the main results presented in this paper.

The work reported in this paper is drawn from several projects that have been developed over the last several years by the NCSA group. The first results for the time evolution of apparent horizons of distorted, nonrotating holes were found by Bernstein [3,4]. Similar techniques were subsequently applied to the two black hole collision [5–7] and the rotating black hole case [8,9]. Early results of this work for the distorted, nonrotating black hole and the two black hole collision, along with color

*Present address: Department of Mathematics, Statistics, and Computing Science, University of New England, Armidale, NSW 2351, Australia.

 ©1994 The American Physical Society

images of the black hole horizons, have appeared with a nontechnical exposition in [10]. In other related work, Abrahams and Evans [11] have investigated the formation of black holes from imploding axisymmetric gravitational waves. In their studies the coordinate position of the apparent horizon undergoes a deformation from prolate to oblate in a time scale that is consistent with the period of the lowest $\ell = 2$ quasinormal mode, confirming the result of Bernstein [3]. The fact that similar behavior has been seen in four rather different spacetimes, with different topologies (the NCSA work is based on one or two Einstein-Rosen bridges and the work of Ref. [11] is based on $\mathbb{R}^3$ topology), indicates the generic nature of these results.

We have developed a number of two-dimensional general relativistic numerical codes to solve the fully nonlinear Einstein equations for axisymmetric vacuum spacetimes containing gravitational waves and black holes. The results we present in this paper were obtained by numerically evolving three distinct families of black hole initial data sets. The first initial data set consists of a single Einstein-Rosen bridge [12] in the presence of a time-symmetric gravitational wave of the form first described by Brill [13]. Properties of this data set and its construction have been described extensively in Refs. [4,14–16]. For our purposes the data set corresponds to an axisymmetric black hole that has been distorted by a ring of gravitational radiation of essentially arbitrary shape and amplitude (up to certain boundary conditions and size restrictions [4,14]). The second family of problems is an extension of the first and includes distorted, rotating black holes, based on a generalization of both the Bowen and York [17] and the Brill wave black hole constructions described above. The third initial data set we consider is the time symmetric, two equal mass black hole set of Misner [18]. This family of initial data sets was evolved by Smarr *et al.* [19–21] in their pioneering studies of black hole collisions, and more recently in Refs. [5–7]. The various families of initial data sets possess different geometries and coordinate systems that are uniquely adapted to these geometries. However, the format of the data and the methods we use to analyze it in both cases are similar and, for the most part, the discussions presented in the following sections are applicable to all three cases with few modifications.

The general framework and a brief outline of the different initial data sets discussed in this paper are presented in Secs. II and III. Section IV provides an overview of apparent horizons in general relativity and introduces measures of mass and geometry that will be used in the following sections. A number of case studies for each family of initial data sets are presented in Sec. V along with a discussion of the dynamical behavior of apparent horizons found in those spacetimes. We summarize our results in Sec. VI.

II. COMPUTATIONAL FRAMEWORK

We use the 3+1 formalism whereby spacetime is viewed as a foliation by three-surfaces each endowed with a positive definite three-metric γ_{ab} and an extrinsic curvature tensor K_{ab}. (In this paper greek indices will range from 0 to 3, latin indices from 1 to 3. We work in geometrized units in which Newton's constant G and the speed of light are equal to unity.) The spacetime metric takes the form

$$ds^2 = -(\alpha^2 - \beta^a\beta_a)dt^2 + 2\beta_a dx^a dt + \gamma_{ab}dx^a dx^b, \quad (1)$$

where α (the "lapse function") determines the foliation of the spacetime and β^a (the "shift vector") specifies three-dimensional coordinate transformations from slice to slice. In numerical relativity calculations it is common to choose the initial data and shift vector to eliminate certain components of γ_{ab} and here we have chosen γ_{12} and γ_{13} to vanish. The γ_{23} term is present only in the rotating case, carrying information about the odd-parity radiation modes present in that system. The resulting hypersurface line element is

$$\begin{aligned} dl^2 &= \gamma_{ab}dx^a dx^b \\ &= \Psi^4\left(Ad\eta^2 + Bd\theta^2 + D\sin^2\theta d\phi^2 + 2F\sin\theta d\theta d\phi\right). \end{aligned} \quad (2)$$

(η, θ, ϕ) are spherical-polar-like coordinates, η is the logarithmic radial coordinate, and (θ, ϕ) the standard spherical polar coordinates on the η = constant two-spheres. The spacetime is assumed to possess an axial Killing vector $(\partial/\partial\phi)$. All the variables we will work with are independent of ϕ. In addition we choose not to evolve the conformal factor Ψ; hence this is a function of η and θ only.

We specify the topology of the t = constant hypersurfaces in the following way: The single nonrotating distorted hole and the single rotating distorted hole are given the "single Einstein-Rosen bridge" $(\mathbb{S}^2 \times \mathbb{R})$ topology familiar from the Schwarzschild and Kerr spacetimes. The two black hole data sets of Misner possess the "double Einstein-Rosen bridge" topology obtained by identifying the bottom sheets of two single bridges. In all three cases we compute each three-metric such that there is an isometry between the top and bottom sheets. The two-surface invariant under the isometry operation is called the throat and consists of one two-sphere in the single bridge case and two disjoint two-spheres in the double bridge case. In all cases we choose the throat to lie on a constant η surface specified by $\eta = \eta_0$. This provides accurate boundary conditions for the numerical metric.

The Einstein equations are simplified when a conformal factor is introduced into the extrinsic curvature in a manner similar to that in Eq. (2). We adopt the following conformal form for K_{ab}:

$$K_{ab} = \Psi^4 H_{ab} \quad (3)$$

$$= \Psi^4 \begin{pmatrix} H_A & H_C & H_E\sin^2\theta \\ H_C & H_B & H_F\sin\theta \\ H_E\sin^2\theta & H_F\sin\theta & H_D\sin^2\theta \end{pmatrix}. \quad (4)$$

The conformal three-metric components and their corresponding conformal extrinsic curvature components are evolved according to the 3+1 decomposition of the Einstein equations. The lapse function α is determined by using the maximal slicing condition $\mathrm{tr}K = 0$. In the two cases where rotation is not present, the shift β^a is chosen to make all the off-diagonal components of the three-metric to vanish. For the more general rotating case the shift is chosen to eliminate γ_{12} and γ_{13}. It is not possible to eliminate both γ_{13} and γ_{23} in general radiating spacetimes (because they contain information about the odd-parity modes) and we choose to maintain a nonvanishing γ_{23}.

Finally, we choose each spacetime to be equatorially plane symmetric as well as axisymmetric and isometric through a throat. The computational domain is thus bounded by the axis ($\theta = 0$), the equator ($\theta = \pi/2$), the isometry surface ($\eta = \eta_0$), and an outer boundary, usually around $\eta = 6$, but due to the logarithmic nature of this coordinate this is far enough that static outer boundary conditions are adequate for the simulations carried out here. The numerical code to evolve the time-symmetric (nonrotating) single bridge data sets has been described extensively in Refs. [15,22] and so we will not discuss our numerical methods here. Modifications to those methods for evolving the single bridge with rotation and the Misner two black hole initial data sets are detailed in Refs. [9] and [6], respectively.

III. INITIAL DATA SETS

Each of the initial data sets we discuss will contain either one or two black holes, the number being determined by the topology of the t = constant hypersurfaces of the spacetimes. In this section we briefly describe some of the geometrical and physical characteristics of each of the data sets.

A. Black hole plus Brill wave

Initial data for the single bridge, nonrotating case is obtained by setting $K_{ab} = 0$ and putting γ_{ab} in a form similar to that studied by Brill [13]

$$ds^2 = \Psi^4 \left[e^{2q} \left(d\eta^2 + d\theta^2 \right) + \sin^2\theta d\phi^2 \right]. \tag{5}$$

In other terms, $A = B = e^{2q}$, $D = 1$, and $F = 0$ in (2). The function $q(\eta, \theta)$ is arbitrary up to boundary conditions, a falloff rate, and a possible restriction in magnitude [14]. One obtains initial data by specifying q and solving the Hamiltonian constraint for the conformal factor Ψ. On a time-symmetric slice the Hamiltonian constraint reduces to the statement that the scalar curvature of γ_{ab} vanishes and using Eq. (5) this becomes

$$\frac{\partial^2\Psi}{\partial\eta^2} + \frac{\partial^2\Psi}{\partial\theta^2} + \cot\theta\frac{\partial\Psi}{\partial\theta} - \frac{\Psi}{4} = -\frac{\Psi}{4}\left(\frac{\partial^2 q}{\partial\eta^2} + \frac{\partial^2 q}{\partial\theta^2} \right). \tag{6}$$

We choose the function $q(\eta, \theta)$ to have the form

$$q(\eta, \theta) = Q_0 g(\eta) \sin^n\theta, \tag{7}$$

where we use the "inversion symmetric Gaussian"

$$g(\eta) = \exp\left[-\left(\frac{\eta + \eta_0}{\sigma} \right)^2 \right] + \exp\left[-\left(\frac{\eta - \eta_0}{\sigma} \right)^2 \right] \tag{8}$$

for the radial function g. Symmetry considerations require n to be a positive, even integer. For these initial data sets the throat is located at $\eta = 0$ and the isometry operation is $\eta \to -\eta$.

The function q has three parameters which, roughly speaking, specify the amplitude (Q_0), range (η_0), and width (σ) of the wave. (We note that in other papers related to this work [14,15] the amplitude is denoted by a, but here we use Q_0 to avoid confusion with the usual angular momentum parameter a that is used in describing rotating black holes in this paper.) One regains the Schwarzschild spacetime by setting $Q_0 = 0$ in which case the Hamiltonian constraint has solution

$$\Psi = \sqrt{2m}\cosh(\eta/2), \tag{9}$$

where m is a length scale parameter which, in this case, is equal to the mass of the hole [and also the Arnowitt-Deser-Misner (ADM) mass of the spacetime].

Some properties of the apparent horizon in these initial data sets are discussed in Sec. V A. For a more thorough discussion the reader is referred to [4,14].

B. Distorted rotating black holes

We extend the discussion of the previous section to include rotating black holes. The interested reader is referred to Refs. [8,9] for a more detailed treatment.

Our discussion begins by writing the Kerr metric [23] in a form that is free of coordinate singularities and which is enough like the form of Eq. (5) that we can make direct comparisons between rotating and nonrotating spacetimes. The transformation that achieves this is

$$r = r_+ \cosh^2(\eta/2) - r_- \sinh^2(\eta/2), \tag{10}$$

$$r_\pm = m \pm \sqrt{m^2 - a^2}, \tag{11}$$

where a is the standard Kerr angular momentum parameter and m is the mass of the Kerr black hole. With this transformation the spatial part of the Kerr metric can be written as

$$ds^2 = \Psi^4 \left[e^{-2q_0} \left(d\eta^2 + d\theta^2 \right) + \sin^2\theta d\phi^2 \right], \tag{12}$$

where

$$\Psi^4 = g^{(K)}_{\phi\phi} / \sin^2\theta, \tag{13}$$

$$e^{-2q_0} = g^{(K)}_{rr} \left(\frac{dr}{d\eta} \right)^2 = g^{(K)}_{\theta\theta}, \tag{14}$$

and $g^{(K)}_{\mu\nu}$ is the Kerr metric in Boyer-Lindquist coordi-

nates [23]. Notice that if $a = 0$, then $q_0 = 0$ and we recover the Schwarzschild three-metric.

We can now generalize the metric (12) to include a Brill wave by adding a function $q(\eta, \theta)$ in a manner similar to Eq. (5):

$$ds^2 = \Psi^4 \left[e^{2(q-q_0)} \left(d\eta^2 + d\theta^2 \right) + \sin^2\theta d\phi^2 \right]. \quad (15)$$

In this context, the parameter q_0 is interpreted as the Brill wave required to make the spacetime conformally flat. This rotating spacetime can be distorted by setting $q = Q_0 g(\eta) \sin^n \theta + q_0$ where $g(\eta)$ is given by Eq. (8).

A consequence of adding the function q to the metric is that Ψ is no longer the analytic form given by Eq. (13), but must be calculated from the Hamiltonian constraint

$$\frac{\partial^2\Psi}{\partial\eta^2} + \frac{\partial^2\Psi}{\partial\theta^2} + \frac{\partial\Psi}{\partial\theta}\cot\theta - \frac{\Psi}{4}$$

$$= -\frac{\Psi}{4}\left(\frac{\partial^2}{\partial\eta^2}(q-q_0) + \frac{\partial^2}{\partial\theta^2}(q-q_0) \right) \quad (16)$$

$$-\frac{\Psi^{-7}}{4}\left(\hat{H}_E^2 \sin^2\theta + \hat{H}_F^2 \right), \quad (17)$$

where we have introduced $\hat{H}_E = \Psi^6 H_E$ and $\hat{H}_F = \Psi^6 H_F$ as a procedure to decouple the Hamiltonian and momentum constraints [17].

Because we use $(t, \phi) \to (-t, -\phi)$ symmetry instead of $t \to -t$ symmetry on the initial slice, the extrinsic curvature components $\hat{H}_E$ and $\hat{H}_F$ are defined to satisfy the momentum constraint

$$\frac{\partial}{\partial\eta}\left(\sin^3\theta \hat{H}_E \right) + \frac{\partial}{\partial\theta}\left(\sin^2\theta \hat{H}_F \right) = 0. \quad (18)$$

Solutions to this equation include $\hat{H}_E = 3J$, $\hat{H}_F = 0$ (i.e., the Bowen-York [17] solution, where J is the total angular momentum of the spacetime) and the Kerr solution. We note that the quantity determining the presence of rotation in our spacetimes is H_E. The angular momentum about the z axis in maximally sliced spacetimes is computed from Eq. (37) to be $J = p_\phi = \oint \hat{H}_E \, d\hat{S}^\eta/(8\pi)$.

C. Two black hole Misner data

Misner [18] derived the following single parameter family of time symmetric ($K_{ab} = 0$) solutions

$$ds^2 = \Psi_M^4 \left(d\rho^2 + dz^2 + \rho^2 d\phi^2 \right), \quad (19)$$

where

$$\Psi_M = 1 + \sum_{n=1}^{\infty} \frac{1}{\sinh(n\mu)} \left(\frac{1}{{}^{+}r_n} + \frac{1}{{}^{-}r_n} \right) \quad (20)$$

and

$${}^{\pm}r_n = \sqrt{\rho^2 + [z \pm \coth(n\mu)]^2}. \quad (21)$$

This solution is topologically two Euclidean sheets joined by two throats representing nonrotating equal mass black holes colliding head on along the z axis. The two throats are defined by $(z_{\rm th} \pm z_0)^2 + \rho_{\rm th}^2 = 1/\sinh^2\mu$ where $z = \pm z_0 = \pm\coth\mu$ are the black hole centers.

The free parameter μ is related to the ADM mass of the spacetime,

$$M = 4\sum_{n=1}^{\infty} \frac{1}{\sinh(n\mu)}, \quad (22)$$

and the proper distance along the spacelike geodesic connecting the throats:

$$L = 2\left[1 + 2\mu \sum_{n=1}^{\infty} \frac{n}{\sinh(n\mu)} \right]. \quad (23)$$

Increasing μ sets the two black holes farther away from one another and decreases the total mass of the system.

Our calculations of colliding black holes are performed using the Čadež coordinates [24] $x^i = (\eta, \theta, \phi)$, defined by the complex transformation

$$\chi(\zeta) = \eta + i\theta$$

$$= \frac{1}{2}\left[\ln(\zeta + \zeta_0) + \ln(\zeta - \zeta_0) \right]$$

$$+ \sum_{n=1}^{\infty} C_n \left(\frac{1}{(\zeta_0 + \zeta)^n} + \frac{1}{(\zeta_0 - \zeta)^n} \right), \quad (24)$$

where $\zeta = z + i\rho$ is the complex combination of cylindrical coordinates and $\zeta_0 = z_0$ defines the black hole centers. The coefficients C_n are determined by a least-squares method to fix the initial throats to lie on an $\eta =$ constant coordinate line. To maintain a clear comparison with the other data sets discussed in this paper we have chosen to use θ in place of the usual ξ, which appears in Refs. [6,7,24], to represent the "angular" coordinate.

The metric in this set of coordinates can be written in the form of Eq. (2) as

$$ds^2 = \Psi^4 \left(d\eta^2 + d\theta^2 + D\sin^2\theta \, d\phi^2 \right), \quad (25)$$

where $\Psi^4 = \Psi_M^4/J$, $D = J\rho^2/\sin^2\theta$ and $J = (\partial\eta/\partial\rho)^2 + (\partial\eta/\partial z)^2$ is the Jacobian of the two coordinate systems.

The advantage of Čadež coordinates is that they are boundary-fitted coordinates designed to conform naturally to the spatial geometry of two black holes. They are spherical near the throats of the holes and further out in the wave zone, thus allowing us to handle throat boundaries and asymptotic wave form extractions in a convenient way. Their disadvantage is a singular point introduced by the coordinate transformation [Eq. (24)] at the origin ($\rho = z = 0$). This presents certain numerical difficulties that will not be discussed here. Instead, we refer the interested reader to Ref. [6] for a thorough discussion of our numerical methods.

IV. APPARENT HORIZONS

Let S be a two-sphere embedded in Σ, a t = constant slice of a spacetime M, and let s^μ be the outward-pointing spacelike unit normal to S in Σ and n^μ the future-pointing timelike unit normal to Σ in M. Thus $k^\mu = n^\mu + s^\mu$ is null and S is called a *marginally trapped surface* (MTS) if

$$\nabla_\mu k^\mu = 0 \tag{26}$$

holds everywhere on S. (We will use ∇_μ for the covariant derivative with respect to the spacetime metric $g_{\mu\nu}$ and D_a for that with respect to γ_{ab}.) The apparent horizon is the outermost MTS and may consist of several disjoint two-spheres (this is the standard definition, e.g., [25]). Equation (26) expresses the condition that null rays emitted normal to the surface have zero volume expansion and it is well known that such a surface (if it exists) must lie inside of an event horizon in any spacetime not containing a naked singularity [1]. Unlike the event horizon, the MTS may be located on a given slice Σ without computing the entire spacetime and in axisymmetry this makes the location of apparent horizons a comparatively simple exercise. A number of researchers have investigated the existence, location, and physical properties of apparent horizons in a variety of initial data sets [14,26–28].

To locate an MTS we write Eq. (26) in terms of the extrinsic curvature of Σ [29]

$$D_a s^a + K_{ab} s^a s^b - \mathrm{tr}K = 0. \tag{27}$$

The unit normal s^a is a function of the first derivative of the coordinate location of the horizon and so Eq. (27) is a second order equation for these coordinates. Specifically we assume the coordinate position of the horizon is of the form $(h(\theta), \theta, \phi)$. This has tangent $t^a = (dh/d\theta, 1, 0)$ and s^a may be computed from the conditions $t^a s_a = 0$ and $s^a s_a = 1$. This form of the horizon is a restriction of the general parametrization of an axisymmetric surface $(h(x), \theta(x), \phi)$. Since the null normal divergence vanishes on the MTS we should not expect it to be highly curved, even in its coordinate representation, because this would tend to make the divergence larger in the highly curved regions. Hence requiring the surface to be single valued in θ is unlikely to prevent a solution of Eq. (27) and in fact we have never encountered a situation in which this appeared to be the case.

Using the above two conditions on s^a and the three-metric (2) we may compute

$$s^a = \frac{\left(1,\ \frac{AD}{F^2 - BD} h_{,\theta},\ 0\right)}{\Psi^2 \sqrt{A + \frac{A^2 D}{BD - F^2}(h_{,\theta})^2}}. \tag{28}$$

Substituting this into Eq. (27) results in a lengthy second order nonlinear ordinary differential equation for $h(\theta)$. We solve this by the method originally used by Cook [28] which consists of finite differencing $h(\theta)$ with the usual second order centered operators and applying the Newton-Raphson root-finding algorithm to solve the resulting set of coupled nonlinear algebraic equations. [The interpolation scheme used to compute the values of the metric and extrinsic curvature components and their derivatives at $h(\theta)$ and other details of our numerical methods can be found in Ref. [4].]

Once the horizon has been found we may compute several standard measures of its intrinsic geometry in order to understand its shape and how it changes in time. In particular, we may compute the embedding diagram of the horizon, its Gaussian curvature κ, and its polar and equatorial circumferences C_p and C_e. In axisymmetry the latter two are well defined since the ϕ = constant curves and the curve $\theta = \pi/2$ are geodesics of the surface. The quantities are

$$C_p = 4 \int_0^{\pi/2} \Psi^2 \sqrt{A \left(\frac{dh}{d\theta}\right)^2 + B + \frac{F^2}{D}}\, d\theta \tag{29}$$

and

$$C_e = 2\pi \Psi^2 \sqrt{D}, \tag{30}$$

evaluated at $\theta = \pi/2$, and we define C_r to be their ratio

$$C_r = \frac{C_p}{C_e}. \tag{31}$$

Calculation of the Gaussian curvature κ of the horizon is performed in a similarly straightforward manner. It can be computed on the horizon surface by the formula

$$\kappa = \frac{\bar{D}'}{2(\bar{B}\bar{D} - \bar{F}^2)^2}(\bar{D}\bar{B}' + \bar{B}\bar{D}' - 2\bar{F}\bar{F}') - \left(\frac{\bar{D}''}{\bar{B}\bar{D} - \bar{F}^2}\right), \tag{32}$$

where

$$\bar{F} = \Psi^4 F \sin\theta, \tag{33}$$

$$\bar{D} = \Psi^4 D \sin^2\theta, \tag{34}$$

$$\bar{B} = \Psi^4 \left[B + A\left(\frac{dh}{d\theta}\right)^2\right], \tag{35}$$

and primes denote derivatives with respect to changes of θ along the horizon surface [i.e., $D' = D_{,\theta}|_\eta + (dh/d\theta) D_{,\eta}|_\theta$].

Typically in our spacetimes the area of the apparent horizon grows with time due to a numerical effect which is well understood but difficult to circumvent [4] [an example is the case of Fig. 10(a)]. This causes the Gaussian curvature of the horizon to decrease with time (since for a sphere the Gaussian curvature is just 4π divided by the area) and we choose to normalize the curvature in the following way. Let A_{AH} and M_{AH} be the proper area and mass of the apparent horizon as defined below [see Eq. (38)]. We compute the angular momentum parameter a/M_{AH} from the known total angular momentum J. From this we compute the Gaussian curvature of the equilibrium solution with that mass and angular momentum parameter (i.e., from the Kerr solution; see Sec. V B for details). With no rotation this is just $4\pi/A_{\mathrm{AH}}$ which is $(2M_{\mathrm{AH}})^{-2}$. We then divide the Gaussian curvature of the

horizon by this equilibrium quantity normalized to 4π. In spherical symmetry, therefore, the "area-normalized Gaussian curvature" will take on the value 4π, independent of the area of the horizon. Henceforth, when we refer to Gaussian curvature, we have normalized it in this way.

We also compute the embedding diagram of the horizon in a flat three-space. We construct a two-surface in the flat space with the same intrinsic geometry as the apparent horizon, thereby obtaining a "picture" of the horizon and its topology (which in this case is fixed). Once it has been determined that the embedding exists, construction of the diagram is obtained by standard methods [30,31]. The embedding diagrams are also "normalized" in a manner similar to the Gaussian curvature, by plotting the flat-space coordinates in units of a characteristic mass which we take to be the ADM mass M (36) [or the apparent horizon mass $M_{\rm AH}$ (38) when numerical effects cause it to become larger than M].

The total mass and angular momentum of the spacetime are evaluated using the ADM integrals [32]

$$M = -\frac{1}{2\pi}\oint_S \nabla_a \Psi dS^a, \tag{36}$$

$$P_a = \frac{1}{8\pi}\oint_S \sqrt{\gamma}\,(K_{ab} - \gamma_{ab}{\rm tr}K)\,dS^b \tag{37}$$

($\gamma = {\rm det}\gamma_{ab}$) at the outer edge of our grid. As long as gravitational waves do not propagate beyond the outer boundary (36) will remain constant. In axisymmetry, with $\partial/\partial\phi$ the Killing vector, the component P_ϕ is the total angular momentum which we denote by J. Gravitational radiation cannot carry angular momentum in axisymmetry and so J should be strictly constant.

As noted above, the apparent horizon will, in general, lie inside the event horizon so that calculating the area of the apparent horizon should provide a lower bound on the area of the event horizon (this is strictly true on a time symmetric slice). We follow Christodoulou [33] and others by defining the mass of the apparent horizon by

$$M_{\rm AH} = \sqrt{\frac{A_{\rm AH}}{16\pi} + \frac{4\pi J^2}{A_{\rm AH}}}, \tag{38}$$

where J is the angular momentum of the spacetime and $A_{\rm AH}$ is the area of the apparent horizon. The mass of the black hole, $M_{\rm BH}$, is defined by replacing $A_{\rm AH}$ by the area of the event horizon in Eq. (38). On a given slice the difference between the mass of the apparent horizon and the ADM mass provides a measure of the size of the black hole(s) relative to that of the remaining gravitational wave energy on the slice. Since we expect the final state of the evolution of any of our initial data sets to be a static or stationary hole plus gravitational radiation propagating to future null infinity, we will have

$$M = M_{\rm BH} + M_{\rm rad}, \tag{39}$$

where $M_{\rm rad}$ is the total time-integrated energy loss through a two-sphere far from the throat(s). If $M_{\rm BH}$ is approximated by the apparent horizon mass [Eq. (38)], then Eq. (39) can be used to obtain an upper bound on the amount of gravitational radiation which reaches future null infinity.

V. RESULTS

A. Black hole plus Brill wave spacetime

We first discuss general properties of the apparent horizon on the initial slice of the single bridge spacetimes with no rotation. We will then select a few representative cases and examine their time evolution. For a more detailed discussion of both the initial data and evolution see [4,14].

The isometry surface ($\eta = 0$) is an extremal area surface and if the amplitude parameter Q_0 is not too large it is also the apparent horizon. For instance, if the range parameter η_0 is set to zero and the width parameter to one, then the apparent horizon is located at the throat if $-0.65 < Q_0 < 3.03$. For Q_0 in this range the apparent horizon is prolate if Q_0 is positive and oblate if Q_0 is negative. The deformation from sphericity can be quite extreme: For $Q_0 = 2$ the ratio of circumferences C_r is 21.9 and for $Q_0 = -0.5$ it is 0.52 (this is *less* than the minimum possible value of $2/\pi$ for axisymmetric surfaces in flat space). If Q_0 is decreased below -0.65 or increased above 3.03 the throat becomes an unstable minimal surface and the apparent horizon occurs outside of it. In these cases the correspondence between the shape of the horizon and the sign of Q_0 is the same except that as $|Q_0|$ becomes larger the horizon becomes *more* spherical rather than less. This is because the coordinate location of the horizon moves further away from $\eta = 0$ as $|Q_0|$ is increased.

When the range parameter η_0 is greater than zero the "wave" part of the initial data moves away from the throat. In these cases, radiative variables such as the Newman-Penrose quantities (in a tetrad aligned with our coordinates; see [4,14]) and the York curvature tensor components exhibit peaks near η_0. Other measures of the curvature such as the Riemann invariant $R_{\mu\nu\alpha\beta}R^{\mu\nu\alpha\beta}$ also have extrema near η_0. In these cases, as one would expect, the Brill wave has to be larger in magnitude to form an apparent horizon outside the throat. So, for instance, in the initial data sets with $\eta_0 = 1$ and $\sigma = 1$ the throat is the apparent horizon unless $Q_0 < -1.42$. In this case the throat and the apparent horizon are minimal area surfaces and there exists an unstable minimal surface in between them.

For the evolution we look at five cases: the three "perturbation" spacetimes

case (1a): $Q_0 = 0.1$, $\eta_0 = 0$, $\sigma = 1.0$, $n = 2$;
case (1b): $Q_0 = 0.1$, $\eta_0 = 0$, $\sigma = 1.0$, $n = 4$;
case (1c): $Q_0 = 0.1$, $\eta_0 = 3$, $\sigma = 0.3$, $n = 2$;

and the two "large amplitude" spacetimes

case (1d): $Q_0 = +1.0$, $\eta_0 = 0$, $\sigma = 1.0$, $n = 2$;
case (1e): $Q_0 = -1.0$, $\eta_0 = 2$, $\sigma = 1.0$, $n = 2$.

Cases (1a) and (1b) study the effect of a small ampli-

tude wave interacting with a hole. The wave is initially centered on the throat, which is the apparent horizon for these two data sets, and this causes a slight initial distortion of the horizon. As discussed in Ref. [14] the $n = 2$ case contains predominantly the $\ell = 2$ angular modes, where ℓ is the index of the spherical harmonic $Y_{\ell m}$, while the $n = 4$ case contains a stronger admixture of the $\ell = 2$ and $\ell = 4$ modes. Case (1c) explores the collision of a low amplitude "wave packet" with an initially spherical hole. Case (1d) is the high amplitude version of case (1a) and case (1e) explores the collision of a high amplitude wave with a hole.

In Fig. 1 we show the evolution of the ratio of circumferences C_r for case (1a). The solid lines represent numerical results, while the dashed lines show a fit to the fundamental and first overtone of the $\ell = 2$ quasinormal mode frequencies known from perturbation theory [34] using the least squares method to choose the phase and amplitude of both modes. We see that the initially distorted hole relaxes to a spherical shape in a damped oscillatory fashion and the "wavelength" $(16.8M)$ and "damping time" $(11.2M)$ of the ratio of circumferences are very close to those of the fundamental $\ell = 2$ quasinormal mode frequency. [In cases (1a)–(1c) the ADM mass is very close to the final apparent horizon mass and we use "M" for both.] Note that the time in Fig. 1 is the coordinate time of the $t =$ constant slices on which the apparent horizon is found. This corresponds to the proper time at the grid edge, where the lapse function is close to unity; in the region where the apparent horizon is located the maximal slicing lapse is in the neighborhood of 0.3. Note also that, strictly speaking, the apparent horizon is a *spacelike* hypersurface that can move discontinuously in space. Hence on each slice it cannot actually be causally connected to the horizon surface on the previous slice. However, in these spacetimes the apparent horizons lie very close to the actual event horizons during this oscillation phase, and so they are close to being causally connected on each slice.

The fact that in these spacetimes the apparent horizon oscillates with the quasinormal frequency of the black hole (with respect to the coordinate time t) can be easily understood. As a perturbing source approaches the hole (in this case a gravitational wave), the background spacetime geometry is disturbed. The quasinormal modes are excited, originating at the peak of the gravitational scattering potential $V(r)$, located outside the horizon at $r = 3M$ [34]. Gravitational waves at the quasinormal frequency are then sent in both directions away from the peak of $V(r)$, towards the horizon on one side and towards null infinity on the other side. Those waves going across the horizon induce a shearing of its surface, causing its geometry to oscillate at the same frequency as the waves. As the lapse function is essentially constant in time from the horizon out to infinity during this oscillation phase, the "background" spacetime is approximately static and spherical. (Although coordinates are falling towards the hole and metric functions are growing in time, the horizon itself is a geometric structure that is static in the spherical limit. Its coordinate location may change as coordinates fall towards the hole, but its geometric position does not.) Under these conditions we expect the horizon to oscillate at the quasinormal frequency in coordinate time as the ingoing waves cross it. Therefore, under many circumstances we expect to be able to use the apparent horizon as a probe to explore the dynamics of the black hole spacetime. The same dynamics have been seen in the geometry of the event horizon, as reported in Ref. [2].

The $n = 4$ case is much the same, and the ratio of circumferences with a similar quasinormal mode fit is shown in Fig. 2. Despite the significant $\ell = 4$ component of the initial data the horizon damps down with approximately the same wavelength and damping time, that of the $\ell = 2$ mode. We can, however, see the presence of the $\ell = 4$ mode in the horizon oscillations. In Fig. 3 we have plotted the difference Δ between the numerically generated C_r and the $\ell = 2$ mode fit. The residual is clearly related to the $\ell = 4$ modes, and a fit of the two lowest such modes is shown. This shows that the oscillations are a superposition of the various multipole quasinormal modes excited when the black hole is disturbed.

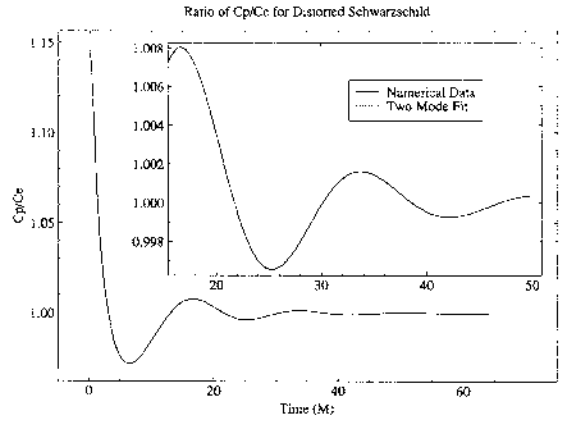


FIG. 1. We show the ratio of polar to equatorial circumferences C_r of the apparent horizon as a function of time for case (1a). The inset shows a least squares fit to the two lowest $\ell = 2$ quasinormal mode frequencies.

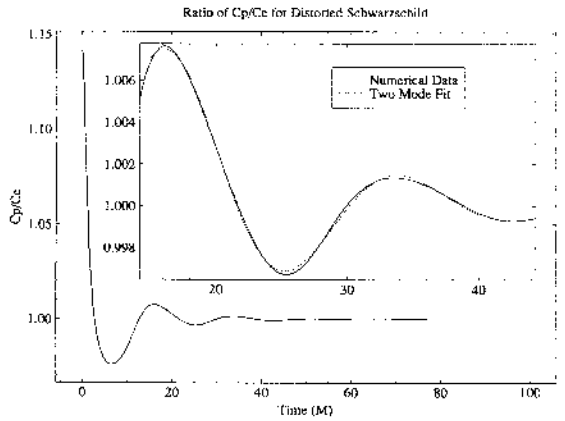


FIG. 2. The ratio of circumferences C_r of the apparent horizon is shown as a function of time for case (1b). The inset shows a least squares fit to the two lowest $\ell = 2$ quasinormal mode frequencies.

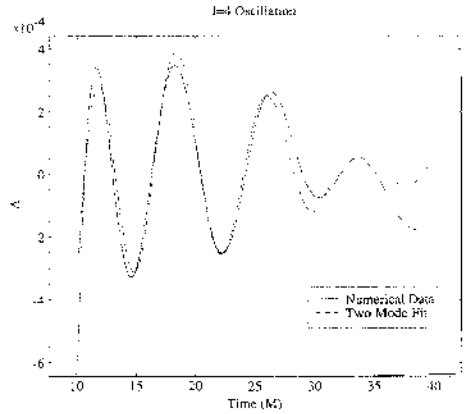


FIG. 3. We plot the quantity Δ, which is the difference between the ratio of circumferences C_r and the $\ell = 2$ mode fit for case (1b). The dotted line is a least squares fit to the two lowest $\ell = 4$ quasinormal mode frequencies.

In Figs. 4 and 5 we show the "area-normalized Gaussian curvature" of the apparent horizon, normalized to its equilibrium value 4π as described in Sec. (IV), as a function of polar angle θ and coordinate time for the two cases (1a) and (1b), respectively. Here the shading is such that the minimum curvature is mapped to white, the maximum is mapped to black, and intermediate values are represented by scales of gray (the equilibrium value 4π is represented by a medium shade of gray). This sensitive map is used to bring out the dynamics as the horizon settles down to its equilibrium shape (which is a sphere for the spacetimes discussed in this section). The $n = 2$ spacetime [case 1(a)] in Fig. 4 has a distinct "box" pattern indicating that the normalized curvature oscillates between greater than and less than 4π around what appears to be a fixed line of latitude on the horizon

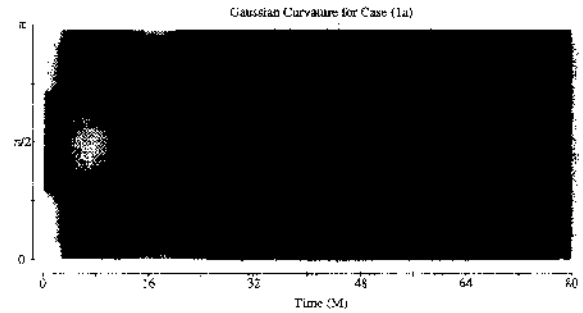


FIG. 4. Gaussian curvature of the apparent horizon is plotted as a function of polar angle θ and coordinate time for case (1a). As discussed in the text, the "box" pattern is typical for the predominantly $\ell = 2$ distortion. The period of the oscillation of $16.8M$ can be seen in the diagram.

which has a value close to $\pi/3$. Consequently there are moments of time where the apparent horizon is momentarily spherical (has constant Gaussian curvature). The $n = 4$ case presented in Fig. 5 is qualitatively different—here we see an "X" pattern: The curvature is not oscillating around a fixed line and there are no moments of constant curvature. Again, one can see that in both cases the characteristic oscillation frequency is close to the $\ell = 2$ normal mode frequency, although in Fig. 5 higher frequencies related to the $\ell = 4$ modes are also visible.

These patterns are distinctive of the different oscillation modes. The box pattern of Fig. 4 is primarily showing the $\ell = 2$ modes and the "X" pattern of Fig. 5 contains an admixture of both $\ell = 2$ and $\ell = 4$. We have verified that these patterns are to be expected for these spacetimes by expanding the metric in terms of a spherical background piece $\overset{\circ}{g}_{\alpha\beta}$ and a nonspherical perturbation piece $h_{\alpha\beta}$, where

$$h_{\alpha\beta} = \begin{pmatrix} \overset{\circ}{g}_{tt}\, H_0 Y_{\ell 0} & H_1 Y_{\ell 0} & h_0 Y_{\ell 0,\theta} & 0 \\ H_1 Y_{\ell 0} & \overset{\circ}{g}_{rr}\, H_2 Y_{\ell 0} & h_1 Y_{\ell 0,\theta} & 0 \\ h_0 Y_{\ell 0,\theta} & h_1 Y_{\ell 0,\theta} & R^2\left(K + G\frac{\partial^2}{\partial\theta^2}\right) Y_{\ell 0} & 0 \\ 0 & 0 & 0 & R^2\left(K\sin^2\theta + G\sin\theta\cos\theta\frac{\partial}{\partial\theta}\right) Y_{\ell 0} \end{pmatrix} \tag{40}$$

is expanded in terms of the Regge-Wheeler perturbation functions $(H_0, H_1, H_2, h_0, h_1, K, G)$, which are all functions of the radial and time coordinates (η, t) only, and the $Y_{\ell 0} = Y_{\ell 0}(\theta)$ are the usual spherical harmonic functions of order ℓ, m, with $m = 0$. We note that in our perturbed spacetimes the apparent horizon lies on approximate constant radial coordinate lines and we can easily compute the Gaussian curvature on such surfaces from the above expansion in terms of the functions G, K and the tensor spherical harmonics. If we assume the perturbation is a superposition of the various ℓ modes, each oscillating at the appropriate quasinormal frequency, we obtain the following expressions for the Gaussian curvature to lowest perturbative order:

$$\kappa_{\ell=2} = \frac{1}{R^2}\left(2 + \frac{K}{2}\sqrt{\frac{5}{\pi}}\,(1 + 3\cos 2\theta)\, e^{-i\omega t}\right) \tag{41}$$

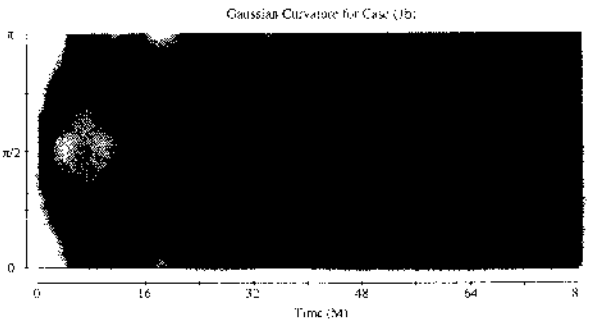


FIG. 5. Gaussian curvature of the apparent horizon is plotted as a function of polar angle θ and coordinate time for case (1b). The characteristic "X" pattern is expected for an admixture of $\ell = 2$ and $\ell = 4$ modes, as shown in the text.

and

$$\kappa_{\ell=4} = \frac{1}{R^2}\left(2 + \frac{27K}{64\sqrt{\pi}}\left(9 + 20\cos 2\theta + 35\cos 4\theta\right)e^{-i\omega t}\right). \tag{42}$$

These expressions generate the characteristic "box" pattern for a pure $\ell = 2$ perturbation and the "X" pattern for an admixture of $\ell = 2$ and $\ell = 4$ perturbations, as expected. From the $\ell = 2$ pattern, there is a line of constant curvature at $\theta = 0.5$ $\arccos(-1/3) \sim \pi/3$, which is observed as noted above. Thus, these diagrams are very useful in identifying the various oscillation modes present in the horizon, as different modes have qualitatively different patterns.

Figure 6 shows C_r for case (1c). Here the initial position of the wave maximum is centered at about Schwarzschild radius $r = 11M$ with width roughly equal to $6M$. From the figure we see that the horizon is initially nearly spherical (with $C_r = 1.0$ at $t = 0$) and remains so until the wave collides with it starting at about $t = 8M$, with the initial peak occurring at about $t = 12M$. The initial wavelength of the oscillation is also about $7M$–$8M$ judging from the position of the first two peaks in the figure. By about $t = 20M$ the horizon has reached its maximum distortion and begins to relax to a sphere again with the $\ell = 2$ quasinormal frequency. This case is similar to the example presented in Ref. [2] where both the event and apparent horizons were shown to oscillate at the normal mode frequency when hit by a gravitational wave.

Case (1d) is the high amplitude version of case (1a). Figure 7 shows the corresponding C_r and the least squares $\ell = 2$ mode fit. The hole is much more distorted initially than case (1a), but almost all of the initial distortion is shed by $t = 5M$ off the initial slice and by about $t = 20M$ or so the hole is oscillating in the $\ell = 2$ mode like the others.

We can also construct a complete geometric embedding of the two-dimensional (2D) horizon surface in a flat 3D space, as described in Sec. IV. Figure 8 shows the horizon embedding for a sequence of time slices. On the initial slice the horizon is quite prolate. The surface quickly evolves towards a more spherical configuration, and then begins to oscillate at the quasinormal frequency about its spherical equilibrium shape, going from slightly oblate to slightly prolate and back, eventually settling down to a sphere. At $t = 40M$ the hole is quite spherical, as shown in the figure.

Similarly, case (1e) is the high amplitude version of (1c). Here the wave is initially closer in and more spread out than in (1c) (for numerical reasons this was necessary). However it retains the basic features of the low amplitude case. Figure 9 shows the ratio of circumfer-

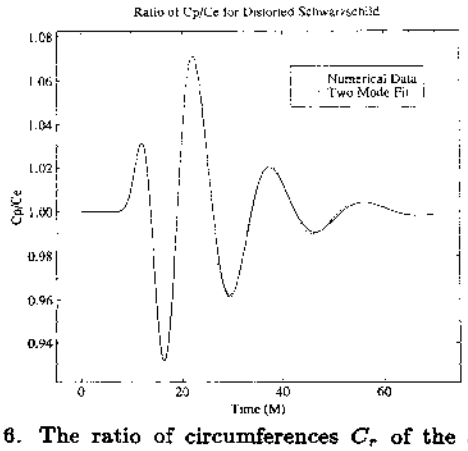


FIG. 6. The ratio of circumferences C_r of the apparent horizon is shown as a function of time for case (1c). Here the initial position of the gravitational wave was away from the throat, but the hole begins to oscillate at its normal mode frequency when hit by the wave.

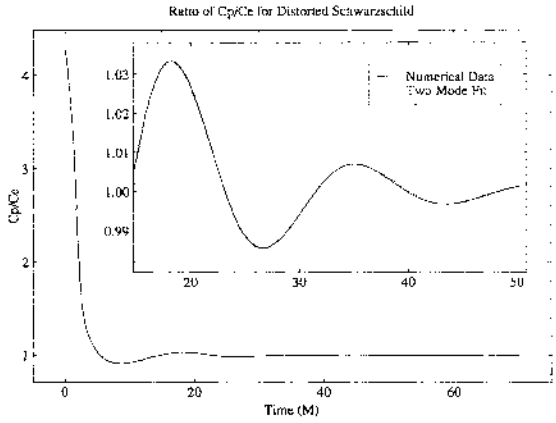


FIG. 7. The ratio of circumferences C_r of the apparent horizon is shown as a function of time for case (1d). The amplitude of the wave is stronger in this case, causing a much stronger distortion of the hole.

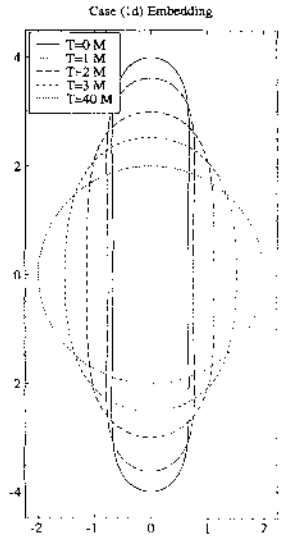


FIG. 8. We show cross sections of the geometric embedding of the horizon in a flat 3D space, at various times, for case (1d). Initially the hole is quite prolate, but it quickly evolves towards a more spherical shape, when it begins to oscillate at the quasinormal frequency of the hole.

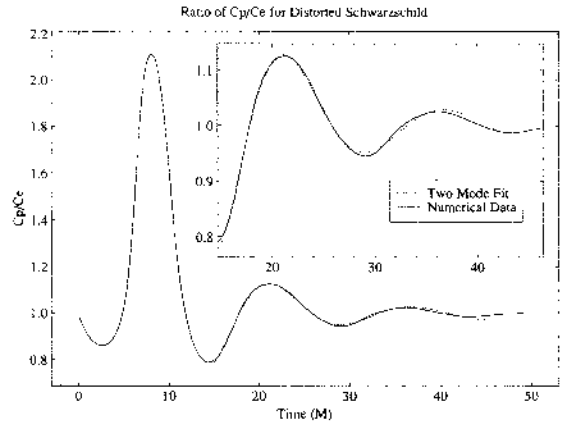


FIG. 9. The ratio of circumferences C_r of the apparent horizon is shown as a function of time for case (1e), which is similar to case (1c) but with a larger amplitude gravitational wave.

ences: The apparent horizon (again initially located at the throat) is more or less spherical at $t = 0$; it then suffers a collision with the wave, in the process absorbing some of the available mass energy of the wave. This collision excites oscillations in the horizon, again with the $\ell = 2$ quasinormal mode frequency, and then it settles to a spherical state.

In Fig. 10 we show the mass of the horizon, defined by Eq. (38), in units of the total ADM mass for the spacetimes of cases (1d) and (1e). The figure shows that in these cases the mass of the horizon increases rapidly as the wave is absorbed by the hole, finally leveling off at approximately $0.993M$ for case (1d) and $0.87M$ for case (1e). Hence for these two cases about 0.7% and 13% of the ADM mass escapes to null infinity, respectively. We note that in cases like these we have been able to account for the energy lost through gravitational radiation via various energy flux formulas (e.g., the Zerilli function and the Newman-Penrose scalar Ψ_4 [22]), providing a consistent accounting of the total energy of the system. As we are focusing on horizon dynamics here, full details of these calculations will be discussed elsewhere. Finally, note that the time derivative of the mass appears to be out of phase with the distortion of the horizon: Just

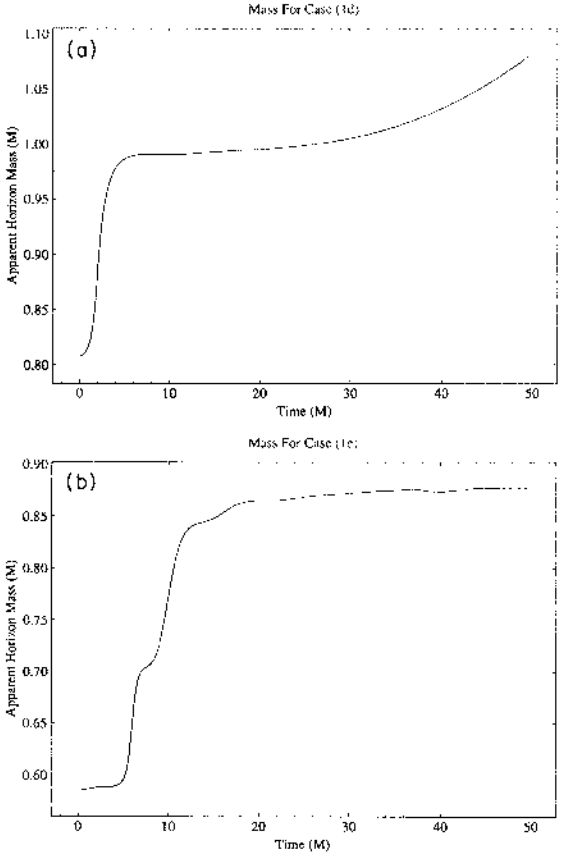


FIG. 10. We show the mass of the apparent horizon $M_{\rm AH}$ as a function of time for cases (1d) (a) and (1e) (b). The mass increases dramatically as the wave is swallowed by the hole.

when the horizon is most distorted (e.g., the peak near $t = 8M$) the mass is momentarily constant.

B. Distorted rotating holes

In this section we discuss evolutions of apparent horizons surrounding a single rotating black hole distorted by Brill waves of varying amplitudes. We consider three separate cases:

$$\begin{aligned}
&\text{case (2a):}\quad Q_0 = 0.1, \quad n = 2, \quad \sigma = 1, \quad \eta_0 = 0, \quad J = 0.5;\\
&\text{case (2b):}\quad Q_0 = 1.0, \quad n = 2, \quad \sigma = 1, \quad \eta_0 = 0, \quad J = 5.5;\\
&\text{case (2c):}\quad Q_0 = 0.1, \quad n = 2, \quad \sigma = 1, \quad \eta_0 = 0, \quad J = 3.5.
\end{aligned}$$

These cases represent black holes of progressively larger values of J/M^2: 0.14, 0.39, and 0.61 for cases (2a), (2b), and (2c), respectively. (We note that J/M^2 is equivalent to a/m in the standard Boyer-Lindquist notation [23].)

All of the simulations reported in this paper use the conformal spatial metric defined by Eq. (15) and the Bowen-York solution to the momentum constraint (18). These data sets can be regarded as distorted versions of the standard Bowen-York solution, as described above. Because the differences in the maximum radiation loss between the distorted Bowen-York solutions and the distorted Kerr solutions are small (< 20% for all cases discussed in this paper), we expect similar evolutions from both types of initial data sets. However, the distorted Bowen-York data sets are somewhat more convenient to work with because one does not need to specify J/M^2 on the initial data set.

In Figs. 11 and 13 we show C_r for cases (2a) and (2c),

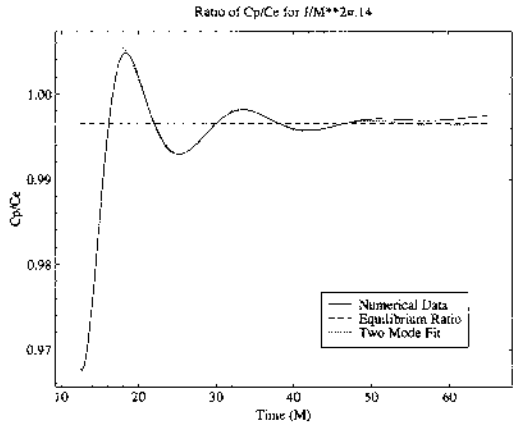


FIG. 11. The ratio of circumferences C_r of the apparent horizon is shown as a function of time for case (2a). This is a rotating version of case (1a). The long dashed line shows the offset required by the quasinormal mode fit, which is related to the rotation of the hole as discussed in the text.

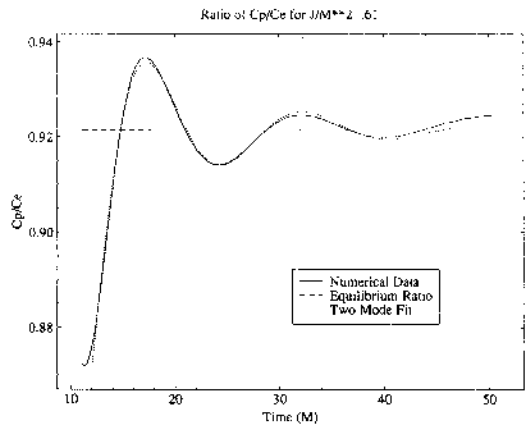


FIG. 13. The ratio of circumferences C_r of the apparent horizon is shown as a function of time for case (2c). This case is similar to case (2a), but with a significantly larger rotation parameter.

respectively. These are rotating versions of the case (1a) discussed in the previous section, with case (2c) having significantly more angular momentum than case (2a). Solid lines represent numerical results, while the short dashed lines show the result of fitting the two lowest $\ell = 2$ quasinormal modes. However, as we explain in the following paragraphs, the holes are not oscillating about $C_r = 1$, as they are in the nonrotating case, but about some other equilibrium value related to their rotation. (We note that the slight upward drifting of C_r at late times is due to the numerical difficulties in computing the area of the horizon as described in Sec. IV and in more detail in Ref. [9].) The long dashed lines denote the value of the constant offset or equilibrium ratio required by the $\ell = 2$ fit to C_r. In Fig. 12 we show results for case (2b) which is a rotating version of case (1d) discussed above. Again, we have computed the fit of the numerical results to the two lowest $\ell = 2$ quasinormal modes, including the offset obtained by the fit. In fitting C_r to the

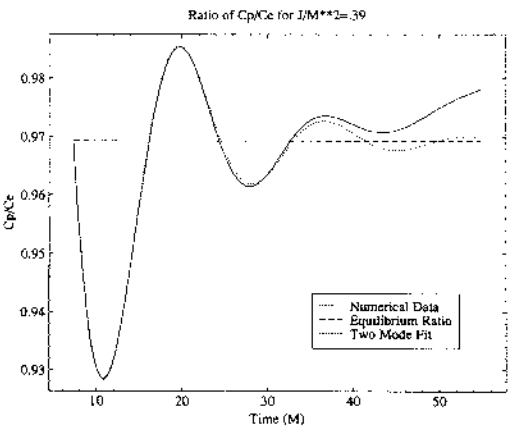


FIG. 12. We show the ratio of circumferences C_r of the apparent horizon as a function of time for case (2b). This is a rotating version of case (1d). The long dashed line shows the offset required by the quasinormal mode fit.

lowest two quasinormal modes we included corrections for the wavelength due to rotation [35]. The quasinormal frequencies of rotating black holes depend on their angular momentum as well as their mass, but the dependence on the angular momentum is extremely weak except for large rotation rates in which $a/m \sim 1$. As a result, corrections due to rotation rates for the cases that we have studied here are slight and they make no significant impact to the fitted wave modes.

It is difficult to determine the angular momentum of the black hole from the wavelength of the quasinormal mode except in cases of extreme rotation. However, one can use the shape of the horizon itself as a much more sensitive probe of rotating black hole spacetimes. For holes with angular momentum, the equilibrium shape of the apparent horizon is not spherical [30], but rather it is oblate. Therefore the equilibrium value of C_r is less than unity, as confirmed by the mode fits described above. The exact value of this parameter for Kerr black holes is a unique function of the rotation parameter $a/M = J/M^2$ [30]. The larger the rotation parameter, the more oblate the horizon becomes, as is evident in Figs. 11–13. This effect provides a means to extract the value of J/M^2 from the apparent horizon. The procedure for doing this begins by computing C_r and its offset from unity and then using the results of Ref. [30] to estimate the rotation parameter, which we denote by $\left(J/M^2\right)_{(C_r)}$. We can also estimate the mass of the hole M from C_e, which allows us to solve for the angular momentum J strictly in terms of measurements of the horizon geometry. Because C_e settles down to $4\pi M$ as the horizon approaches equilibrium, we can represent $C_e/4\pi$ as $M_{(C_e)}$. Then J is computed by the formula

$$J = \left(J/M^2\right)_{(C_r)} M^2_{(C_e)}, \tag{43}$$

which works well throughout the evolution.

We find that the value of J extracted from the horizon surface by using this procedure is identical to the input parameter specified solving the momentum constraint to

within a few percent for all cases studied. Therefore, simply by making measurements of the geometric shape of the horizon we can accurately estimate the mass and angular momentum of the black hole. Alternatively, in cases like this where we know the angular momentum of the hole, specified in an initial value procedure, we can measure the shape of the horizon, compute the offset value of the oscillations, and compare with the analytic results of Ref. [30]. However, in a more general three-dimensional case, where angular momentum can be radiated by gravitational waves, the angular momentum of the hole cannot be known as an input parameter, but could still be estimated in this way.

In Fig. 14 we show the evolution of the Gaussian curvature κ for the apparent horizon in case (2c). The oscillatory pattern is similar to the the nonrotating case (1a), but there are some differences. First, we note that because the rotating hole is not spherical, the equilibrium curvature is not a constant over the surface as in the nonrotating case. Next we note that because rotating black holes are not spherical, the small numerically induced deviations of J/M^2 from its initial value, due to the effect described above, combined with the low amplitude of the oscillations at late times, complicates the normalization of κ described in Sec. (IV) above. Therefore the oscillations are difficult to observe at late times. Finally, in all of our simulations of rotating black holes the horizon jumps discontinuously at an early time [$\sim 10M$ for case (2c) shown in Fig. 14]. As described in more detail in Ref. [8], we use a lapse that vanishes on the throat of the hole. For evolutions that use such a lapse the surface $\eta = 0$ is always a MTS. This means that a second MTS must form for two reasons. First, the hole will be gaining mass energy as it absorbs gravitational radiation, and its area must increase. Second, the horizon's shape must change to that of the stationary Kerr hole when it settles down [36–38]. The discontinuous jump in the apparent horizon location indicates that a second MTS surface has formed outside the $\eta = 0$ surface. This effect is responsible for the "frozen" Gaussian curvature at early times.

Finally, in Fig. 15 we show the embedding of the horizon for the case (2c) at the initial time and at $t = 40M$ when the hole has settled down. Initially, the hole is somewhat prolate, whereas at late times it settles down

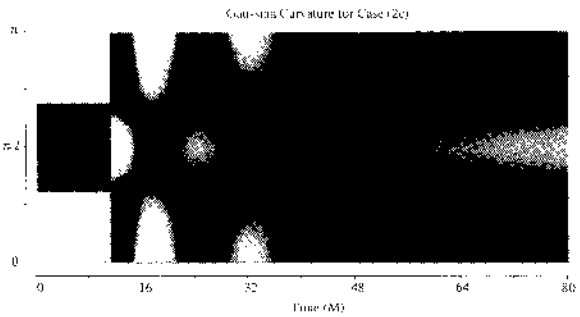


FIG. 14. The Gaussian curvature κ of the apparent horizon is plotted as a function of polar angle θ and coordinate time for case (2c).

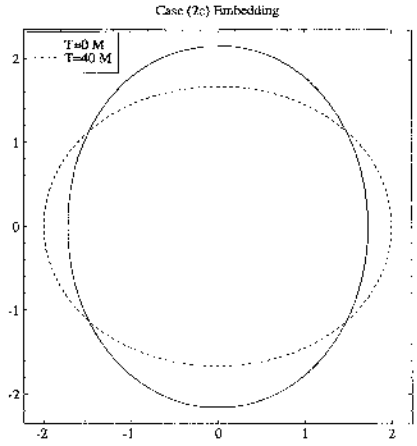


FIG. 15. A cross section of the horizon embedding in a flat three-dimensional space is shown for case (2c) at the initial time $t = 0$ and at a late time $t = 40M$. The hole settles to an oblate state at late times, as discussed in the text.

to a visibly oblate state, as expected according to the discussion above.

C. Colliding black holes

We conclude this section with a discussion of the results found in evolving the Misner initial data set for the collision of two equal mass black holes. Here we focus only on the dynamics of the apparent horizons. The results for the two black hole spacetimes presented here are discussed in much more detail in Refs. [5,7]. There one can also find more general discussions of the total energies radiated, observed gravitational wave forms, horizon masses, ..., for a variety of initial configurations as defined by the parameter μ.

On the initial time-symmetric slice, the isometry surfaces in the Misner data sets are minimal area surfaces and therefore marginally trapped surfaces. When the holes are sufficiently close together, another minimal area surface forms to surround both throats and the evolutions in these cases are that of single perturbed black holes. To simulate the collision process, it is important to know at what values of the parameter μ we expect this behavior to occur. Smarr, Čadež, and co-workers [19] calculated the critical value μ_c that allows a single connected minimal area surface to surround both holes to be $\mu_c \sim 1.362$. For values $\mu < 1.362$, the Misner initial data represent single distorted black holes and for $\mu \gg 1.362$, two colliding black holes. Although for $\mu > 1.362$ the apparent horizons are separate initially, we expect a single event horizon to surround both holes until the holes reach some critical separation, which we estimate to occur at $\mu \sim 1.8$, based on studies of the event horizons of these spacetimes [2].

We present the results from two cases:

$$\text{case (3a):} \quad \mu = 1.2 \quad (L/M = 2.23);$$
$$\text{case (3b):} \quad \mu = 2.2 \quad (L/M = 4.46);$$

sampling both regimes of parameter space. L/M is the

proper distance between the two throats in units of the total ADM mass of the spacetime. (We note that the characteristic unit of mass used here differs from that in Refs. [5–7] where we normalize physical quantities relative to the "mass" of a single black hole $M/2$.) We have verified that case (3b) represents two distinct black holes by integrating photons out along the equator ($z = 0$) from the origin ($z = \rho = 0$), making certain they propagate freely to $\rho \to \infty$ and are not trapped within the event horizon that forms to surround both holes during the merger process. The actual event horizon of this spacetime has been traced out and discussed in Ref. [2].

In Figs. 16 and 17 we plot C_r as a function of time for cases (3a) and (3b), respectively. We use solid lines to represent the numerical results and dashed lines for the fits to the two lowest $\ell = 2$ quasinormal modes. The horizon begins in a highly prolate state [or in case (3b), the first observed merged horizon is highly prolate]. But in a very short time, much less than the damping time due to the quasinormal ringing, the two holes evolve to a configuration that can be regarded as a perturbation of the final, equilibrium spherical black hole. At this point the quasinormal ringing of the final hole sets in.

We note that C_r is computed using the "equatorial" circumference at $\theta = \pi/2$. However, for the horizons surrounding disjoint black holes such as case (3b) at early times, the coordinate $\theta = \pi/2$ extends through the axis ($\rho = 0$) of the two surfaces and not their equatorial plane as would be the case for horizons that extend across the equator to cover both black holes. As a result, C_r as we have defined it is infinite for disjoint surfaces because $C_e = 0$. For this reason we plot in Fig. 17 only the evolution for times greater than $t \sim 8M$, which corresponds to the time our code first computes a global horizon for case (3b). The value of C_r at this time is ~ 2.2. In general, larger initial separations between the two colliding black holes result in greater horizon distortions as evidenced in the plots of C_r. One can draw comparisons between these colliding black hole calculations and the single black hole distortions discussed in Sec. V A. For example, case (3b) is intermediate between cases (1a) and (1d) in terms of the initial merged horizon distortions. A more relevant comparison can be made with a Brill wave perturbation of amplitude $Q_0 \sim 0.56$ which displays similar behavior in the initial horizon distortions, the damping time to relax to the subsequent quasinormal mode ringing, and in the amplitude of the mode ringing.

Figure 18 shows the embedding diagrams for case (3b) at various times as the horizon evolves from an initially disjoint configuration to a nearly static spherical state. The embeddings of case (3a), not shown here, are similar to the merged horizon embeddings of case (3b) but with less initial distortion. At the initial time slice, the disjoint apparent horizons in Fig. 18 are the two throat positions. Because we use a lapse that is zero on both throats (as in the rotating black hole simulations), each throat remains a MTS throughout the evolution with a

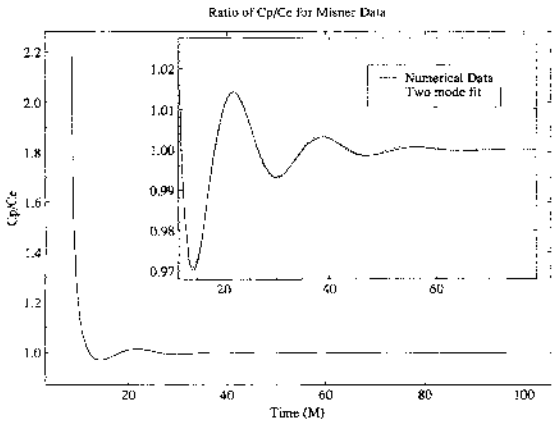


FIG. 17. The ratio of circumferences C_r of the apparent horizon is shown as a function of time for case (3b). The inset shows a least squares fit to the two lowest $\ell = 2$ quasinormal mode frequencies.

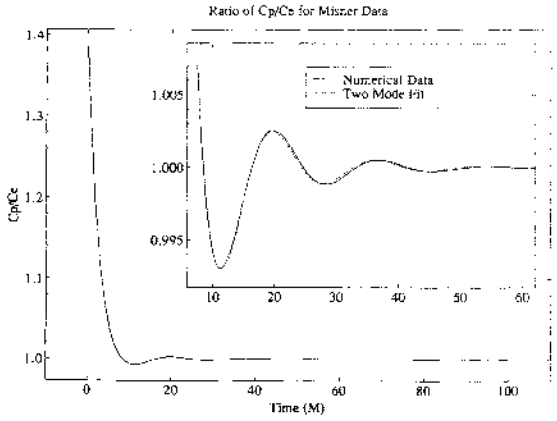


FIG. 16. The ratio of circumferences C_r of the apparent horizon is plotted as a function of time for case (3a). The inset shows a least squares fit to the two lowest $\ell = 2$ quasinormal mode frequencies.

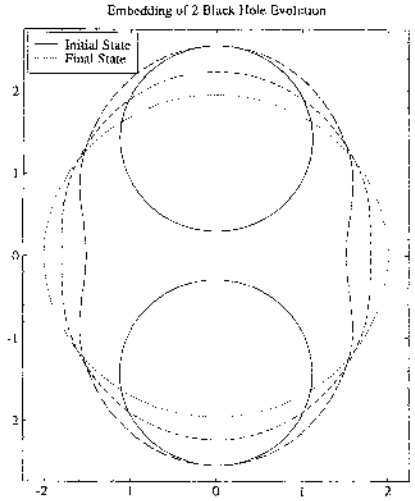


FIG. 18. We show the cross section of the horizon embedding for the two black hole collision case (3b). At late times the final single black hole reaches a nearly static, spherical state.

"frozen" intrinsic geometry. Our code does not distinguish among the different MTS's that may form outside the throats except where such surfaces intersect the equator ($z = 0$). As a result, the embedding diagrams remain constant in time until $t \sim 8M$ when the disjoint surfaces merge to form a single common horizon. The embeddings after the merger are normalized by the computed mass of the apparent horizon $M_{\rm AH}$ as described in Sec. IV. However, to maintain a sense of the relative scale of the initial two black holes to the final coalesced single hole, we choose to normalize the coordinates of the embedding diagrams before the merger ($t < 8M$) by the total ADM mass M. The amount of energy lost to gravitational radiation in this case is only a small fraction (0.06%) of the total ADM mass of the spacetime. Hence we have $M \sim M_{\rm BH} \sim M_{\rm AH}$ at late times after the holes have merged and the normalization applied during the infall phase using the ADM mass is a reasonable choice as compared to using the mass of a single initial apparent horizon, $0.79M$.

We do not present figures of the Gaussian curvature for cases (3a) and (3b), but merely note that they are similar to case (1a) as represented by Fig. 4. The dynamical evolution of the (merged) horizons is similar to the moderately distorted, $n = 2$, Brill wave perturbation of a single nonrotating black hole. The characteristic oscillation frequency is predominantly the $\ell = 2$ normal mode frequency. There is very little $\ell = 4$ signal in the oscillations.

VI. DISCUSSION

From the results presented in Sec. V, we can draw striking similarities between the $n = 2$ Brill wave perturbations of single rotating and nonrotating black holes and the collision of two equal mass black holes. The features common to the variety of spacetimes we have evolved include the following: (1) the initially highly distorted prolate and/or oblate horizon geometries quickly damp away towards an equilibrium shape (which is spherical for nonrotating holes and oblate for rotating holes), (2) the horizon oscillates at a frequency that is predominantly the $\ell = 2$ quasinormal mode frequency of the final state (or mass) of the black hole, and (3) these oscillations damp away in time as the black hole emits gravitational radiation. The frequency and damping time of these oscillations can be found by examining oscillations in the apparent horizon two-geometry. In fact, the consistency in our results over a range of various spacetimes with different time slicings (although all cases are maximal, the rotating and colliding black hole spacetimes use a lapse that is antisymmetric across the throat while the nonrotating single black hole spacetimes use a lapse that is symmetric across the throat) suggests that all dynamic horizon geometries should have some generic features in common, particularly at late times when the dynamics are dominated by the quasinormal ringing of the holes.

The fact that the horizons oscillate at the quasinormal mode frequency can be understood from the standard picture of black hole perturbation theory. A disturbance in the gravitational field of a black hole generates gravitational waves at the peak of the gravitational scattering potential $V(r)$, which is located near $r = 3M$. These waves, emitted at the quasinormal frequency of the hole, propagate away from the peak, down the hole on one side and away from the hole on the other side of the potential peak. The ingoing waves cause both a shearing and expansion of the black hole horizon, causing it to oscillate at the quasinormal frequency.

We have shown that the apparent horizon can act as a powerful tool in understanding the dynamics of numerically generated black hole spacetimes. Measurements of its intrinsic geometry reveal not only the quasinormal mode frequency of the hole, but also its mass and rotation parameter. The latter effect is particularly important, as the quasinormal mode frequency is so weakly dependent on the rotation parameter that it is extremely difficult to extract from the oscillations themselves. On the other hand, the geometric shape of the horizon is sensitive to the rotation parameter, and can be used to extract information about the angular momentum of the hole. Furthermore, the oscillations in the Gaussian curvature of the horizon two-surface can be used to see at a glance the various ℓ modes present in the oscillation, as different modes have qualitatively different visual features.

The similarities between the colliding black hole simulations and the distorted single hole spacetimes indicate that the latter spacetimes are able to mimic the intermediate and late time behavior of the collision of two black holes. The distorted single black hole spacetimes will continue to be explored as a guide to the physics of black hole collisions, without the complications introduced for studying the head-on two black hole collision.

We have also shown in Ref. [2] that the event horizons of the various black hole spacetimes studied in this paper behave in a similar manner to the apparent horizons. The properties of event horizons will be explored in detail in future publications.

ACKNOWLEDGMENTS

We are pleased to acknowledge our colleagues who have contributed a number of helpful discussions throughout this work, including Andrew Abrahams, Joan Massó, and Wai-Mo Suen. These calculations were performed on the Cray Y-MP at NCSA and the C-90 and the Pittsburgh Supercomputing Center. This work has been supported by NCSA. Some animations and color images of horizon embedding diagrams for spacetimes such as the ones presented in this paper are available on the NCSA relativity group World Wide Web server. The URL for our server is http://jean-luc.ncsa.uiuc.edu.

[1] S. W. Hawking, in *Black Holes*, edited by C. DeWitt and B. S. DeWitt (Gordon and Breach, New York, 1973).
[2] P. Anninos, D. Bernstein, S. Brandt, J. Libson, J. Massó, E. Seidel, L. Smarr, W.-M. Suen, and P. Walker (unpublished).
[3] D. Bernstein, in *Second Texas Symposium on Three-Dimensional Numerical Relativity*, Austin, Texas, edited by R. Matzner (University of Texas, Austin, 1991).
[4] D. Bernstein, Ph.D. thesis, University of Illinois Urbana-Champaign, 1993.
[5] P. Anninos, D. Hobill, E. Seidel, L. Smarr, and W.-M. Suen, Phys. Rev. Lett. **71**, 2851 (1993).
[6] P. Anninos, D. Hobill, E. Seidel, L. Smarr, and W.-M. Suen, NCSA Technical Report No. TR024 (unpublished).
[7] P. Anninos, D. Hobill, E. Seidel, L. Smarr, and W.-M. Suen (in preparation).
[8] S. Brandt and E. Seidel (in preparation).
[9] S. Brandt and E. Seidel (in preparation).
[10] P. Anninos, M. Bajuk, D. Bernstein, D. Hobill, E. Seidel, and L. Smarr, IEEE Comp. Graphics Appl. **13**, 12 (1993).
[11] A. Abrahams and C. Evans, Phys. Rev. D **46**, R4117 (1992).
[12] A. Einstein and N. Rosen, Phys. Rev. **48**, 73 (1935).
[13] D. S. Brill, Ann. Phys. (N.Y.) **7**, 466 (1959).
[14] D. Bernstein, D. Hobill, E. Seidel, and L. Smarr, this issue, Phys. Rev. D **50**, 3760 (1994).
[15] D. Bernstein, D. Hobill, E. Seidel, L. Smarr, and J. Towns, Phys. Rev. D (to be published).
[16] D. Bernstein and K. P. Tod, Phys. Rev. D **49**, 2808 (1994).
[17] J. Bowen and J. W. York, Phys. Rev. D **21**, 2047 (1980).
[18] C. Misner, Phys. Rev. **118**, 1110 (1960).
[19] L. Smarr, A. Čadež, B. DeWitt, and K. Eppley, Phys. Rev. D **14**, 2443 (1976).
[20] L. Smarr, in *Sources of Gravitational Radiation*, edited by L. Smarr (Cambridge University Press, Cambridge, England, 1979), p. 245.
[21] L. Smarr, Ph.D. thesis, University of Texas, Austin, 1975.
[22] P. Anninos, D. Bernstein, D. Hobill, E. Seidel, L. Smarr, and J. Towns, *Numerical Astrophysics* (Springer-Verlag, New York, in press).
[23] C. W. Misner, K. S. Thorne, and J. A. Wheeler, *Gravitation* (W. H. Freeman, San Francisco, 1973).
[24] A. Čadež, Ph.D. thesis, University of North Carolina at Chapel Hill, 1971.
[25] S. W. Hawking and G. F. R. Ellis, *The Large Scale Structure of Spacetime* (Cambridge University Press, Cambridge, England, 1973).
[26] N. T. Bishop, Gen. Relativ. Gravit. **14**, 717 (1982).
[27] A. Čadež, Ann. Phys. (N.Y.) **83**, 449 (1974).
[28] G. Cook, Ph.D. thesis, University of North Carolina at Chapel Hill, Chapel Hill, North Carolina, 1990.
[29] J. York, in *Frontiers in Numerical Relativity*, edited by C. Evans, L. Finn, and D. Hobill (Cambridge University Press, Cambridge, England, 1989).
[30] L. L. Smarr, Phys. Rev. D **7**, 289 (1973).
[31] K. Eppley, Phys. Rev. D **16**, 1609 (1977).
[32] N. O'Murchada and J. York, Phys. Rev. D **10**, 2345 (1974).
[33] D. Chrsitodoulou, Phys. Rev. Lett. **25**, 1596 (1970).
[34] S. Chandrasekhar, *The Mathematical Theory of Black Holes* (Oxford University Press, Oxford, 1983).
[35] E. Seidel and S. Iyer, Phys. Rev. D **41**, 374 (1990).
[36] W. Israel, Phys. Rev. **164**, 1776 (1967).
[37] W. Israel, Commun. Math. Phys. **25**, 152 (1972).
[38] B. Carter, Phys. Rev. Lett. **26**, 331 (1971).

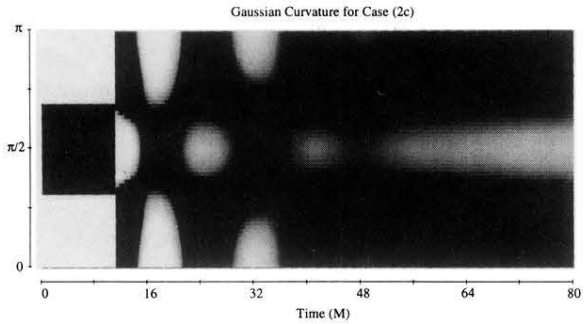


FIG. 14. The Gaussian curvature κ of the apparent horizon is plotted as a function of polar angle θ and coordinate time for case (2c).

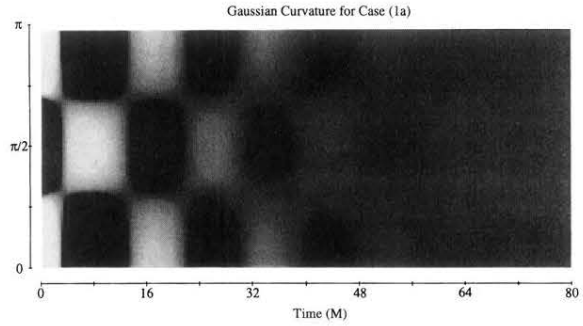


FIG. 4. Gaussian curvature of the apparent horizon is plotted as a function of polar angle θ and coordinate time for case (1a). As discussed in the text, the "box" pattern is typical for the predominantly $\ell = 2$ distortion. The period of the oscillation of $16.8M$ can be seen in the diagram.

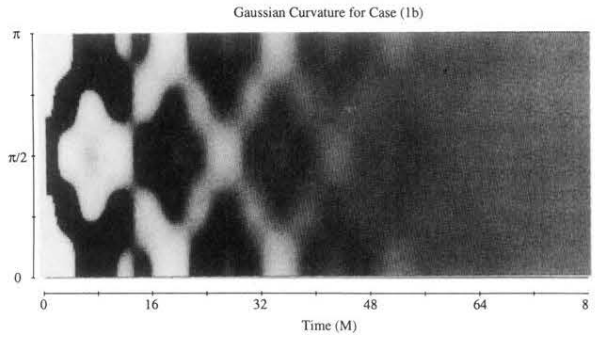


FIG. 5. Gaussian curvature of the apparent horizon is plotted as a function of polar angle θ and coordinate time for case (1b). The characteristic "X" pattern is expected for an admixture of $\ell = 2$ and $\ell = 4$ modes, as shown in the text.